Optical micro-scale mapping of dynamic biomechanical tissue properties

Xing Liang[1], Amy L. Oldenburg[1], Vasilica Crecea[2], Eric J. Chaney[1], and Stephen A. Boppart[1*]

[1]*Department of Electrical and Computer Engineering, Beckman Institute for Advanced Science and Technology, University of Illinois at Urbana-Champaign, 405 N. Mathews Avenue, Urbana, IL 61801, USA*
[2]*Department of Physics, Beckman Institute for Advanced Science and Technology, University of Illinois at Urbana-Champaign, 405 N. Mathews Avenue, Urbana, IL 61801, USA*
[*]*Corresponding author: boppart@uiuc.edu*

Abstract: Mechanical forces such as adhesion, shear stress and compression play crucial roles in tissue growth, patterning and development. To understand the role of these mechanical stimuli, it is of great importance to measure biomechanical properties of developing, engineered, and natural tissues. To enable these measurements on the micro-scale, a novel, dynamic, non-invasive, high-speed optical coherence elastography (OCE) system has been developed utilizing spectral-domain optical coherence tomography (OCT) and a mechanical wave driver. Experimental results of OCE on silicone phantoms are in good agreement with those obtained from a standardized indentation method. Using phase-resolved imaging, we demonstrate OCE can map dynamic elastic moduli of normal and neoplastic *ex vivo* human breast tissue with a sensitivity of 0.08%. Spatial micro-scale mapping of elastic moduli of tissue offers the potential for basic science and clinical investigations into the role biomechanics play in health and disease.

©2008 Optical Society of America

OCIS codes: (110.4500) Optical coherence tomography; (120.5820) Scattering measurements; (120.5050) Phase measurement; (170.6935) Tissue characterization.

References and links

1. Y. C. Fung, *Biomechanics: Mechanical Properties of Living Tissue* (Springer-Verlag New York, Inc., 1993).
2. B. Shraiman, "Mechanical feedback as a possible regulator of tissue growth," Proc Natl. Acad. Sci. USA **102,** 3318-3323 (2005).
3. B. Kim, J. Nikolovski, J. Bonadio, and D. J. Mooney, "Cyclic mechanical strain regulates the development of engineered smooth muscle tissue," Nat. Biotechnol. **17,** 979-983 (1999).
4. L. Gao, K. J. Parker, R. M. Lerner, and S. F. Levinson, "Imaging of the elastic properties of tissue - A review," Ultrasound Med. Biol. **22,** 959-977 (1996).
5. J. Ophir, S. K. Alam, B. S. Garra, F. Kallel, E. E. Konofagou, T. Krouskop, C. R. B. Merritt, R. Righetti, R. Souchon, S. Srinivasan, and T. Varghese, "Elastography: imaging the elastic properties of soft tissues with ultrasound," J. Med. Ultrasonics **29,** 155-171 (2002).
6. I. Céspedes, J. Ophir, H. Ponnekanti, and N. Maklad, "Elastography – elasticity imaging using ultrasound with application to muscle and breast *in-vivo*," Ultrason. Imaging **15,** 73-88 (1993).
7. J. Bercoff, S. Chaffai, M. Tanter, L. Sandrin, S. Catheline, M. Fink, J. L. Gennisson and M. Meunier, "*In vivo* breast tumor detection using transient elastography," Ultrasound Med. Biol. **29,** 1387-1396 (2003).
8. E. J. Chen, J. Novakofski, W. K. Jenkins, and W. D. Jr. O'Brien, "Young's modulus measurements of soft tissues with application to elasticity imaging," IEEE Trans. Ultrason. Ferroelectr. Freq. Control. **43,** 191–194 (1996).
9. A. L. McKnight, J. L. Kugel, P. J. Rossman, A. Manduca, L. C. Hartmann and R. L. Ehman, "MR Elastography of breast cancer: preliminary results," Am. J. Roentgenol. **178,** 1411–1417 (2002).
10. L. S. Wilson, D. E. Robinson, and M. J. Dadd, "Elastography - the movement begins," Phys. Med. Biol. **45,** 1409–1421 (2000).
11. R. Sinkus, M. Tanter, S. Catheline, J. Lorenzen, C. Kuhl, E. Sondermann, and M. Fink, "Imaging anisotropic and viscous properties of breast tissue by magnetic resonance-elastography," Magn. Reson. Med. **53,** 372–387 (2005).
12. J. G. Fujimoto, "Optical coherence tomography for ultrahigh resolution *in vivo* imaging," Nat. Biotechnol. **21**, 1361-1367 (2003).

13. D. Huang, E. A. Swanson, C. P. Lin, J. S. Schuman, W. G. Stinson, W. Chang, M. R. Hee, T. Flotte, K. Gregory, C. A. Puliafito, and J. G. Fujimoto, "Optical coherence tomography," Science **254,** 1178-1181(1991).
14. G. J. Tearney, S. A. Boppart, B. E. Bouma, C. Pitris, M. E. Brezinski, J. F. Southern, E. A. Swanson, and J. G. Fujimoto, "*In vivo* endoscopic optical biopsy with optical coherence tomography," Science **276,** 2037-2039 (1997).
15. M. Wojtkowski, V. Srinivasan, T. Ko, J. Fujimoto, A. Kowalczyk, and J. Duker, "Ultrahigh-resolution, high-speed, Fourier domain optical coherence tomography and methods for dispersion compensation," Opt. Express **12,** 2404-2422 (2004).
16. J. M. Schmitt, "OCT elastography: imaging microscopic deformation and strain of tissue," Opt. Express **3** 199-211 (1998).
17. T. S. Ralston, D. L. Marks, P. S. Carney, and S. A. Boppart, "Interferometric synthetic aperture microscopy," Nat. Phys. **3,** 129-134 (2007).
18. T. S. Ralston, D. L. Marks, S. A. Boppart, and P. S. Carney, "Inverse scattering for high-resolution interferometric microscopy," Opt. Lett. **31,** 3585-3587 (2006).
19. R. Huber, D. C. Adler, and J. G. Fujimoto, "Buffered Fourier domain mode locking: unidirectional swept laser sources for optical coherence tomography imaging at 370,000 lines/s," Opt. Lett. **31,** 2975-2977 (2006).
20. A. S. Khalil, R. C. Chan, A. H. Chau, B. E. Bouma, and M. M. R. Kaazempur, "Tissue elasticity estimation with optical coherence elastography: Toward mechanical characterization of *in vivo* soft tissue," Ann. Biomed. Eng. **33,** 1631-1639 (2005).
21. G. Van Soest, F. Mastik, N. de Jong, and A. F. W. van der Steen, "Robust intravascular optical coherence elastography by line correlations," Phys. Med. Biol. **52,** 2445-2458 (2007).
22. J. Rogowska, N. A. Patel, J. G. Fujimoto, and M. E. Brezinski, "Optical coherence tomographic elastography technique for measuring deformation and strain of atherosclerotic tissues," Heart **90,** 556-562 (2004).
23. H. Ko, W. Tan, R. Stack, and S. A. Boppart, "Optical coherence elastography of engineered and developing tissue," Tissue Eng. **12,** 63-73 (2006).
24. R. K. Wang, S. J. Kirkpatrick, and M. Hinds, "Phase-sensitive optical coherence elastography for mapping tissue microstrains in real time," Appl. Phys. Lett. **90,** 164105 (2007).
25. S. J. Kirkpatrick, R. K. Wang and D. D. Duncan, "OCT-based elastography for large and small deformations," Opt. Express **14,** 11585-11597 (2006).
26. J. M. Schmitt, S. H. Xiang, and K. M. Yung, "Speckle in optical coherence tomography," J. Biomed. Opt. **4,** 95-105 (1999).
27. B. W. Pogue, and M. S. Patterson, "Review of tissue simulating phantoms for optical spectroscopy, imaging and dosimetry," J. Biomed. Opt. **11,** 041102 (2006).
28. E. Dimitriadis, F. Horkay, J. Maresca, B. Kachar, and R. Chadwick, "Determination of elastic moduli of thin layers of soft material using the atomic force microscope," Biophys. J. **82,** 2798–2810 (2002).
29. L. Wang, Y. Wang, S. Guo, J. Zhang, M. Bachman, G. P. Li and Z. Chen, "Frequency domain phase-resolved optical Doppler and Doppler variance tomography," Opt. Commun. **242,** 345-350 (2004).
30. A. Samani, J. Bishop, C. Luginbuhl, and D. B. Plewes, "Measuring the elastic modulus of *ex vivo* small tissue samples," Phys. Med. Biol. **48,** 2183–2198 (2003).
31. E. E. W. Van Houten, M. M. Doyley, F. E. Kennedy, J. B. Weaver, and K. D. Paulsen, "Initial *in vivo* experience with steady-state subzone-based MR elastography of the human breast," J. Magn. Reson. Imaging. **17,** 72-85 (2003).
32. R. Sinkus, J. Lorenzen, D. Schrader, M. Lorenzen, M. Dargatz, and D. Holz, "High-resolution tensor MR elastography for breast tumour detection," Phys. Med. Biol. **45,** 1649–1664 (2000).
33. J. Zhou, J. and L. L. Hsiung, "Biomolecular origin of the rate-dependent deformation of prismatic enamel," Appl. Phys. Lett. **89,** 051904 (2006).
34. P. Frank, *Introduction to System Sensitivity Theory* (Academic Press, INC., 1978).

1. Introduction

Mechanical forces play a significant role in biological tissue development, organization, and response to stimuli. Biomechanical properties of living tissues and engineered tissues depend on their molecular building blocks which can shape and modify the cellular and extracellular structures under stress [1]. For example, forces of adhesion between layers of cells are known to regulate the extracellular growth of tissues [2] and cyclic mechanical strain regulates the development of engineered smooth muscle tissues [3]. Furthermore, pathological changes in the tissue micro-structure such as tumor invasion will lead to different biomechanical properties in tissues. To detect such alterations in soft tissues, physicians for centuries have routinely used palpation as a qualitative method. However, to investigate and quantitatively measure biomechanical properties of tissue as indicators of tissue health and disease, investigators have utilized biomedical imaging technologies.

Elastography is, by definition, an imaging technology which measures tissue elastic properties [4]. Elastography techniques have been developed for the major whole-body or organ-level imaging modalities such as ultrasound and MRI [5-9]. Typical imaging resolutions for ultrasound and MRI elastography are on the order of hundreds of microns [10] and millimeters [11], respectively, which are suitable for tissue-scale imaging. Optical coherence elastography (OCE) is a novel elastography technology used to determine tissue biomechanical properties utilizing the *in vivo* imaging modality optical coherence tomography (OCT) [12-15]. The concept of OCE is similar to ultrasound elastography except that it requires an external force to mechanically stimulate soft tissues [16]. Compared with ultrasound elastography and MRI elastography, OCE can be performed with higher resolution, on the order of several microns throughout the sample volume [17, 18], and higher speed, with acquisition rates as high as 370,000 lines/s [19]. With this cellular-level resolution and several millimeters of imaging penetration into highly-scattering tissues, OCE has the unique ability to non-invasively measure tissue biomechanical properties *in vivo* and on the micro-scale.

Conventional OCE technology has been used to perform intravascular imaging [20, 21], atherosclerotic tissue imaging [22], and imaging of engineered and developing tissues [23]. Phase-resolved measurement methods were also used in OCE technology [24, 25]. However, these earlier studies inherited difficulties from static elastography as they were based on speckle tracking, which has an intrinsic limitation. The speckle pattern is determined by the interference between the scatterers inside the coherence volume [26]. So in conventional OCE, a speckle may not have the same signal amplitude or shape before and after deformation of the sample. Thus, it was difficult for conventional OCE to provide quantitative elastography based on a cross-correlation of speckles on the micro-scale. In this paper, we report micro-scale optical mapping of biomechanical properties of tissues based on a dynamic optical coherence elastography method in which tissue is excited by mechanical waves, and the biomechanical properties can be obtained by solving the wave equations, without the need for computationally expensive cross-correlations. Quantitative measurements of elastic moduli were obtained from tissue phantoms and from *ex vivo* human tissues.

2. Materials and methods

2.1 OCE setup

Our OCE system is derived from a spectral-domain OCT imaging system. In this system, the low-coherence light source consists of a Nd:YVO$_4$-pumped titanium:sapphire laser, which has a center wavelength of 800 nm and a bandwidth of 100 nm, providing an axial resolution of 3 µm in the tissue phantoms. A 12.5 mm diameter 40 mm focal length lens was used in the sample arm to provide a transverse resolution of 13 µm. The average power incident on the samples was 10 mW. A line camera was used to detect the spectral interference signal with an acquisition rate of 25 kHz. As shown in Fig. 1, a glass window stage was fixed in the sample arm of the OCE system to restrict the upper boundary of the tissue phantoms and tissues, yet enable optical imaging through the window. The sample stage was mounted on a mechanical wave driver (SF-9324, PASCO scientific, Roseville, CA), which provided a frequency range of 0.1 Hz to 5 kHz and a maximum amplitude of 7 mm at 1 Hz, decreasing with increasing frequency. The driving waveform was programmed and synchronized with the image acquisition. Samples were mounted between the upper glass window and the sample stage, which are both of larger transverse size than the tissue phantom or tissue samples, with only minimal contact and force prior to data acquisition. To perform M-mode (motion mode, repetitive axial depth-scans into the tissue, acquired at a fixed transverse position over time) OCE, optical backscattering signals were acquired through the upper glass window while the driving mechanical perturbations were exerted simultaneously through the sample stage, compressing the sample vertically. Step and 20 Hz sinusoidal waveforms were used in the OCE experiments.
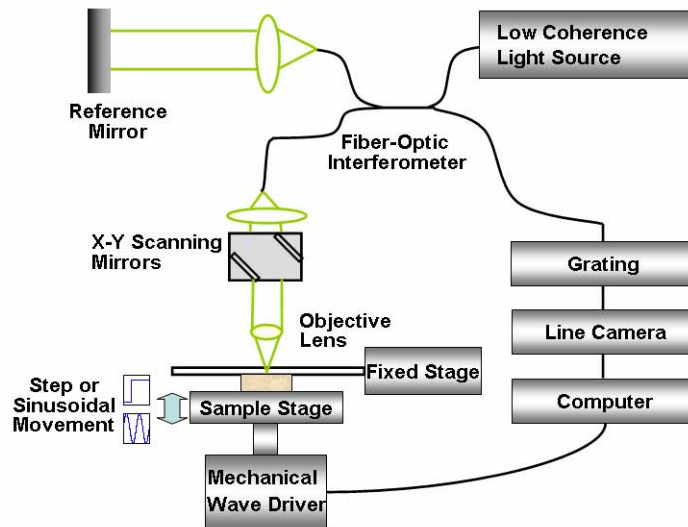
Fig. 1. Schematic diagram of the OCE system. In the OCE system the sample stage is driven upward by the mechanical wave driver, compressing the tissue against a fixed optically-transparent window. Step- or sinusoidally-driven mechanical displacements are synchronized with the OCE acquisition system. For M-mode measurements, the X-Y scanning mirrors remain stationary during acquisition.

2.2 Tissue phantom preparation

Tissue phantoms with similar optical scattering and biomechanical properties as real tissues were used to calibrate the elastic moduli measurements obtained with OCE. Silicone-based tissue phantoms were chosen due to their permanence and the ability to vary their elastic moduli [27]. Phantoms were fabricated from pure polydimethylsiloxane (PDMS) fluid (50 cSt viscosity, ClearCo, Inc.), a room- temperature vulcanizing silicone, and its associated curing agent (General Electric RTV-615 A and B, respectively, Circuit Specialists, Inc.). To obtain different elastic moduli, a series of phantoms were fabricated with different concentration ratios of these three ingredients, which are listed in Table 1. Titanium dioxide (TiO_2) powder (Sigma-Aldrich, #224227, mean size 1 µm, <5 µm) were embedded with a concentration of 1 mg/g in the tissue phantoms to function as optical scatterers for OCE imaging. The phantom solutions were mixed thoroughly in an ultrasonicator for 30 minutes at room temperature and then poured into 35 mm plastic Petri dishes, with a thickness of approximately 10 mm. All phantoms were cured at 80°C for 8 hours and subsequently at room temperature for 24 hours. Two groups of phantoms were fabricated identically for measurement by indentation and by OCE. The silicone tissue phantoms were sectioned into cubes of dimension approximately 10mm × 16mm × 10mm (x-y-z directions).

2.3 Human tissue preparation

Human tissue samples were acquired from breast cancer patients under protocols approved by the institutional review boards of the University of Illinois at Urbana-Champaign and Carle Foundation Hospital, Urbana, Illinois. The tumors were diagnosed by a board-certified pathologist as invasive ductal carcinomas via standard pathological evaluation techniques performed at Carle Foundation Hospital. All human tissues were resected into cubic shapes smaller than the sample stage and upper glass window, placed in a buffered saline solution, and stored in a cooler until imaging was performed within 2 hours.

2.4 Elastic moduli measurements by the indentation method

Bounded indentation experiments were used to independently determine the elastic moduli of one group of the tissue phantoms. A steel sphere with radius of 6.35 mm and a TA.XT Plus Texture Analyzer (Texture Technologies Corp., Algonquin, IL) were used to perform the measurements. With an indenter velocity of 0.01 mm/s and displacement of 2 mm, the measurements were performed for two cycles for each tissue phantom under room temperature. A corrected Hertz contact mechanical model was used to calculate the elastic moduli [28].

2.5 Modeling and elastic moduli measurements of tissue phantoms by OCE

A dynamic OCE system shown in Fig. 1 was used to accurately measure the elastic moduli of tissue samples. To account for the characteristics of the mechanical wave driver and its mechanical coupling with the tissue, a Voigt body including a non-negligible mass was used to model the mechanical wave driver with a spring constant k_0 and a coefficient of viscosity γ_0 as shown in Fig. 2(a). To quantify k_0 and γ_0, M-mode OCE was performed directly on the sample stage without any sample for 0.4 s. This process can be described by

$$m\ddot{z}_{ss}(t) + \gamma_0 \dot{z}_{ss}(t) + k_0 z_{ss}(t) = F(t), \tag{1}$$

in which m is the mass of sample stage, $z_{ss}(t)$ is the displacement of the sample stage from the equilibrium value, and $F(t)$ is the driving step or sinusoidal force. Using M-mode OCE imaging, we extracted the displacement $z_{ss}(t)$ of the sample stage using a third order spline interpolation and peak value detection, and then fitted the curve to the solution to Eq. (1)

$$z_{ss}(t) = Re^{\lambda t} \cos(\mu t - \delta) \tag{2}$$

using least-squares algorithm, where R is the amplitude of the vibration, $\lambda = -\gamma_0 / 2m$ is the damping coefficient, $\mu = \sqrt{4mk_0 - \gamma_0^2} / 2m$ is the damped oscillation frequency of the mechanical wave driver, and δ is a phase factor. The spring constant k_0 and the coefficient of viscosity γ_0 of the wave driver can then be determined. Now that the wave driver has been characterized, one can consider its coupling with the tissue samples. The sample was modeled as a Voigt body coupled to the mechanical wave driver as shown in Fig. 2(b). Tissue phantoms composed of silicone with varying stiffness were investigated using M-mode OCE. Fig. 3(c) is a representative M-mode OCE image of a silicone tissue phantom with a step driving force applied.
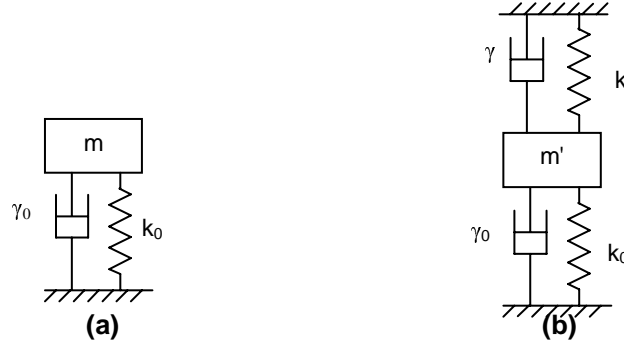
Fig. 2. Schematic diagram of sample models. (a) Voigt body model for the mechanical wave driver. (b) Voigt body models for mechanical wave driver coupled to tissue or silicone phantom.

From the acquired backscattered data, the damped motion of a single scattering particle was selected and displayed in the magnified image in Fig. 3(d). In this figure, the dashed line denotes the driving waveform and the solid line denotes the fitted curve based on the track of the particle motion, which is shown between the dashed and solid curves. The model therefore can be described by

$$m'\ddot{z}_{sp}(t) + (\gamma_0 + \gamma)\dot{z}_{sp}(t) + (k_0 + k)z_{sp}(t) = F(t), \tag{3}$$

where k is the spring constant of the sample, γ is the coefficient of viscosity of the samples, m' denotes the total mass of the sample stage and sample, and $z_{sp}(t)$ now denotes the displacement of the selected scattering particle from the equilibrium value. For M-mode OCE data, the depths of detection are usually less than 1 mm and compared with the heights of the samples, the differences in displacement over our regions of interest can be neglected in terms of fitting the Voigt model. In the same way, one can calculate k_0+k from the fitted parameters of Eq. (3) solution, and finally solve the elastic modulus of the sample using the Hookean strain-stress relationship

$$E_s = kL/S = [(\mu^2 + \lambda^2)m' - k_0]L/S, \tag{4}$$

where L and S are the thickness and the contact area of the samples, respectively. E_s represents the elastic modulus measured by the step-driven OCE. From Eq. (4), we can see that E_s is calculated from the oscillation frequency and damping coefficient of the scattering particle while amplitude information of the oscillation is not needed.
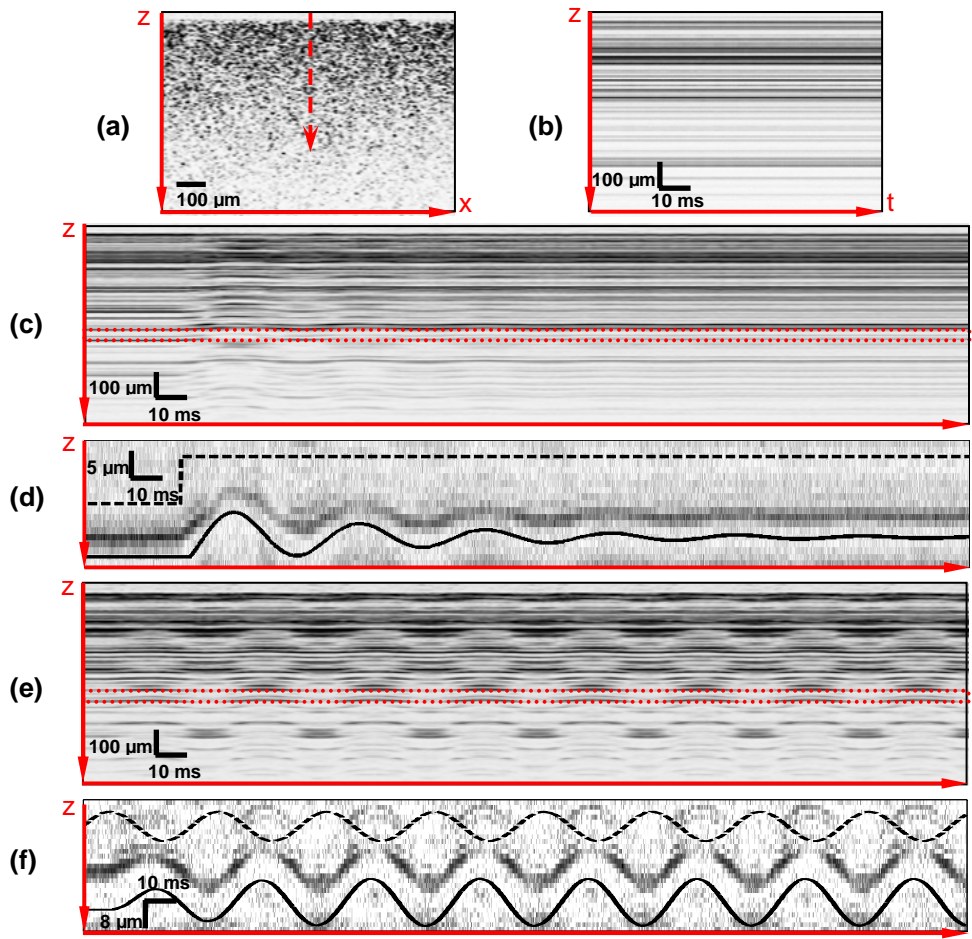
Fig. 3. OCE images of silicone tissue phantoms. (a) B-mode OCT image of a representative silicone tissue phantom. Dashed arrow denotes the position of the laser beam for M-mode OCT imaging. (b) M-mode OCT image of the silicone tissue phantom at the laser beam position in (a). (c) M-mode OCE image with a step-driven waveform. (d) Zoomed-in image of the dotted range in (c). The dashed line represents the driving waveform and the solid line represents the fitted curve, while the image data between the curves shows the scattering particle movement. (e) M-mode OCE image with a sinusoidally-driven waveform. (f) Zoomed-in image of the dotted range in (e). The dashed line represents the driving waveform (amplitude rescaled) and the solid line represents the fitted curve, while the image data between the curves is due to the scattering particle movement.

It is also possible to perform OCE measurement using a sinusoidal driving waveform. Figure 3(e) is an OCE image of the silicone tissue phantom under sinusoidal excitation. In Fig. 3(f), a magnified region of one particle is shown, along with a plot of the driving wave form and fitted curve. The solution to Eq. (3) then becomes

$$z_{sp}(t) = Re^{\lambda t}\cos(\mu t - \delta) + D\sin(\omega t - \alpha), \tag{5}$$

where D is the amplitude for the driving wave and α is another phase factor with η and δ having the same meaning as before. By fitting the experimental data to Eq. (5), the elastic modulus measured by sinusoidally-driven OCE (E_m) can be described by

$$E_m = kL/S = [(\omega^2 - \frac{2\omega\lambda}{\tan\alpha})m' - k_0]L/S \;, \qquad (6)$$

where E_m represents the elastic modulus measured by the sinusoidally-driven OCE.

2.6 Phase-resolved method used for OCE

A phase-resolved method was used to measure the displacements in sinusoidally-driven OCE experiments. Phase-resolved OCE was employed because it was somewhat difficult to extract and track the motion of a single scatterer in optically dense tissue, such as the neoplastic human breast tissue. The theoretical principle of the phase-resolved OCE method is similar to Doppler OCT [29]. When the sample is moving, the Doppler shift and thus the displacement of the scatterers within the laser beam are directly proportional to the interferometric phase angle change between two successive camera exposures. This phase-resolved OCE method has been shown to have higher sensitivity than amplitude-based OCE methods [24]. Silicone tissue phantoms were measured by sinusoidally-driven phase-resolved OCE and the results were verified to be the same as previous amplitude-based OCE results. Then heterogeneous tissue with both tumor and normal adipose regions was imaged by sinusoidally-driven phase-resolved OCE to show the ability to distinguish and spatially map different biomechanical regions in human tissue on the micro-scale. In these experiments, sinusoidal M-mode OCE phase data were recorded for every transverse position of the tissue, which can then be represented as a B-mode (Brightness mode, two-dimensional mode with cross-sectional transverse scanning) OCE image. Each set of M-mode phase data represents the motion track of the scatters within the beam column. By scanning the laser beam transversely across the sample in steps of 15 μm, OCE data was obtained for every pixel within a two-dimensional tissue cross-section, with acquisition time of about 5 s for each frame. Subsequently, calculations were performed for each pixel to generate a 2D spatial map of the elastic moduli. Approximately, the computation time is 7 s for each pixel and 10 hours for a 2D spatial map. Compared with the amplitude-based OCE method, phase-resolved OCE is more sensitive to small displacements of scatterers in the tissue, providing sub-nanometer displacement sensitivity [25].

3. Results and discussion

3.1 OCE results from silicone phantoms

Measured elastic moduli using these two dynamic OCE methods and the commercial indentation method from different silicone concentration ratios are shown in Table 1 and plotted in Fig. 4. In this figure, it is observed that as the mass concentration ratio of the cross-linked to fluid silicone increases, the elastic modulus measured by OCE increases linearly with the one measured by indentation method. Since the indentation method is a standardized way of measuring the elastic modulus of soft tissues, the elastic moduli data by OCE methods are calibrated with the indentation method data according to Fig. 4.

Table 1. Measured elastic moduli for tissue phantoms.

Phantom Concentration Ratio[a]	1:10:10	1:10:20	1:10:30	1:10:50	1:10:80	1:10:100
E_i(kPa)[b]	248.50± 0.42	112.20± 0.19	70.16± 0.12	44.38± 0.12	20.89± 0.04	14.58± 0.03
E_s(kPa)	359.18± 0.30	167.33± 0.48	92.29± 0.17	45.08± 0.17	18.35± 0.13	12.74± 0.16
E_m(kPa)	282.90± 12.51	106.14± 5.80	73.6± 8.57	23.32± 3.11	10.47± 1.12	8.55± 3.90

[a]Concentration ratio of the phantom is the mass ratio of PDMS curing agent RTV-615 B : PDMS RTV-615 A: pure PDMS fluid. [b]E_i stands for the elastic modulus measured by the indentation method while E_s and E_m stand for the elastic moduli measured by step-driven OCE and sinusoidally-driven OCE, respectively.
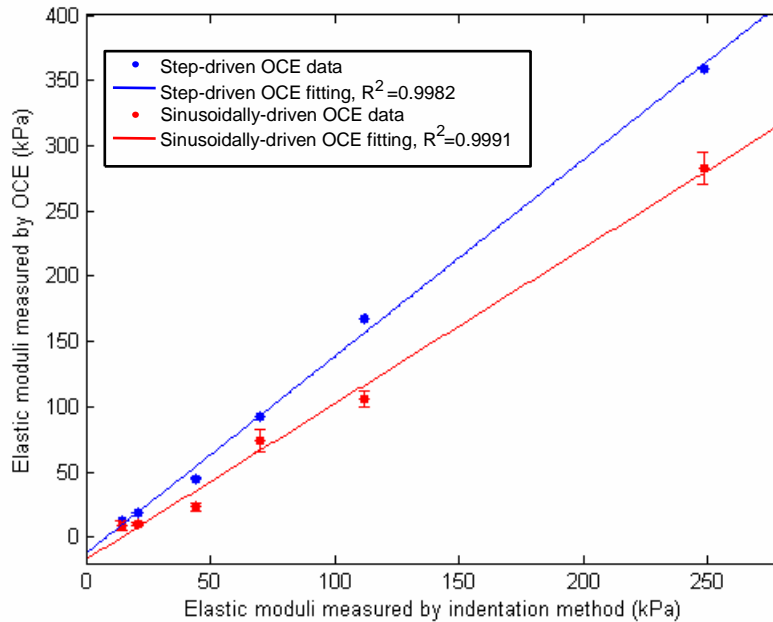

Fig. 4. Measured elastic moduli results by three methods. Measured elastic moduli results with error bars were acquired from step-driven and sinusoidally-driven OCE methods. Measurements were from silicone tissue phantoms of different mass concentration ratios of pure PDMS fluid to the cross-linking PDMS GE-RTV-615 A. Measurements are calibrated with the results from a standard commercial indentation method.

3.2 OCE results from human tissues

Normal and neoplastic *ex vivo* human breast tissues were investigated using dynamic OCE and were modeled using the same process as for the silicone tissue phantoms. The calculations

of elastic moduli were also determined in the same manner. Both tumor and normal adipose tissue were investigated using the sinusoidally-driven OCE method and their elastic moduli were subsequently determined, which are shown in Table 2. From these results, we can see that tumor tissue has an elastic modulus about 25 times larger than that of adipose tissue. Furthermore, tissue samples containing a more heterogeneous combination of tumor and adipose tissue were similarly tested to demonstrate micro-scale optical mapping of elastic moduli using OCE. Images from tissue containing both tumor and normal adipose regions are shown in Fig. 5. Figure 5(a) shows a B-mode OCT image with adipose tissue on the left side and tumor tissue on the right side. This corresponds with the histological image shown in Fig. 5(b). At different transverse positions, the sinusoidally-driven OCE experiments were performed on the sample to test the spatial elastic modulus variation. Elastic moduli measured at 5 different transverse positions are shown in Table 2. In Figs. 5(b) to 5(e), two of the OCE images and associated magnified regions are shown, at positions indicated in Fig. 5(a) by the dotted arrows. When testing tissue containing multiple types, we can discern a large variation of elastic moduli between the tumor and adipose tissue regions, with micro-scale spatial resolution, because each region exhibits different biomechanical properties. However, due to the fact that our current mechanical model does not account for the direct coupling between regions with different moduli, these values are only relative. These OCE results agree well with other *ex vivo* indentation measurements on breast tissue, in which normal adipose and tumor tissues are reported to have elastic moduli of 1.9 kPa and 12 kPa, respectively [30]. Our results also agree with *in vivo* MRI elastography results for tumor tissues, which were reported to have elastic moduli in the range of 2 to 37 kPa, varying with different measurements. For normal adipose tissue, our measured moduli are lower than most of the values reported from *in vivo* MRI elastography studies [31,32], possibly because our measurements were performed *ex vivo*.

Table 2. Measured elastic moduli for human breast tumor tissue.

Tissue type[a]/ Measurement Position[b]	tumor	adipose	t&a[c]/ -1.5mm	t&a/ -1.1mm	t&a / 0mm	t&a / 0.7mm	t&a / 1.2mm
E_s(kPa)	10.68± 0.86	0.42± 0.17	4.14± 5.78	2.69± 2.04	4.59± 4.62	12.92± 4.15	14.15± 3.45

[a]Sinusoidally-driven OCE experiments investigating three types of tissue: tumor tissue only, adipose tissue only, and the combination of tumor and adipose tissues. [b]Measurement positions are corresponding to the transverse positions in Fig. 5(a). [c]T&a indicates the combination of tumor and adipose tissues.

3.3 Results using the phase-resolved method

Using the phase-resolved OCE method, we derived an elasticity map of tissue containing both tumor and normal adipose, as shown in Fig. 6. The B-mode OCT image of the breast tissue is shown in Fig. 6(a), along with the corresponding histology image shown in Fig. 6(b). The measured elasticity map is shown in Fig. 6(c) along with the elasticity error map shown in Fig. 6(d). In Figs. 6(c) and 6(d), white areas denote pixels with OCE signals smaller than an amplitude threshold, and median filtering was performed on both images.
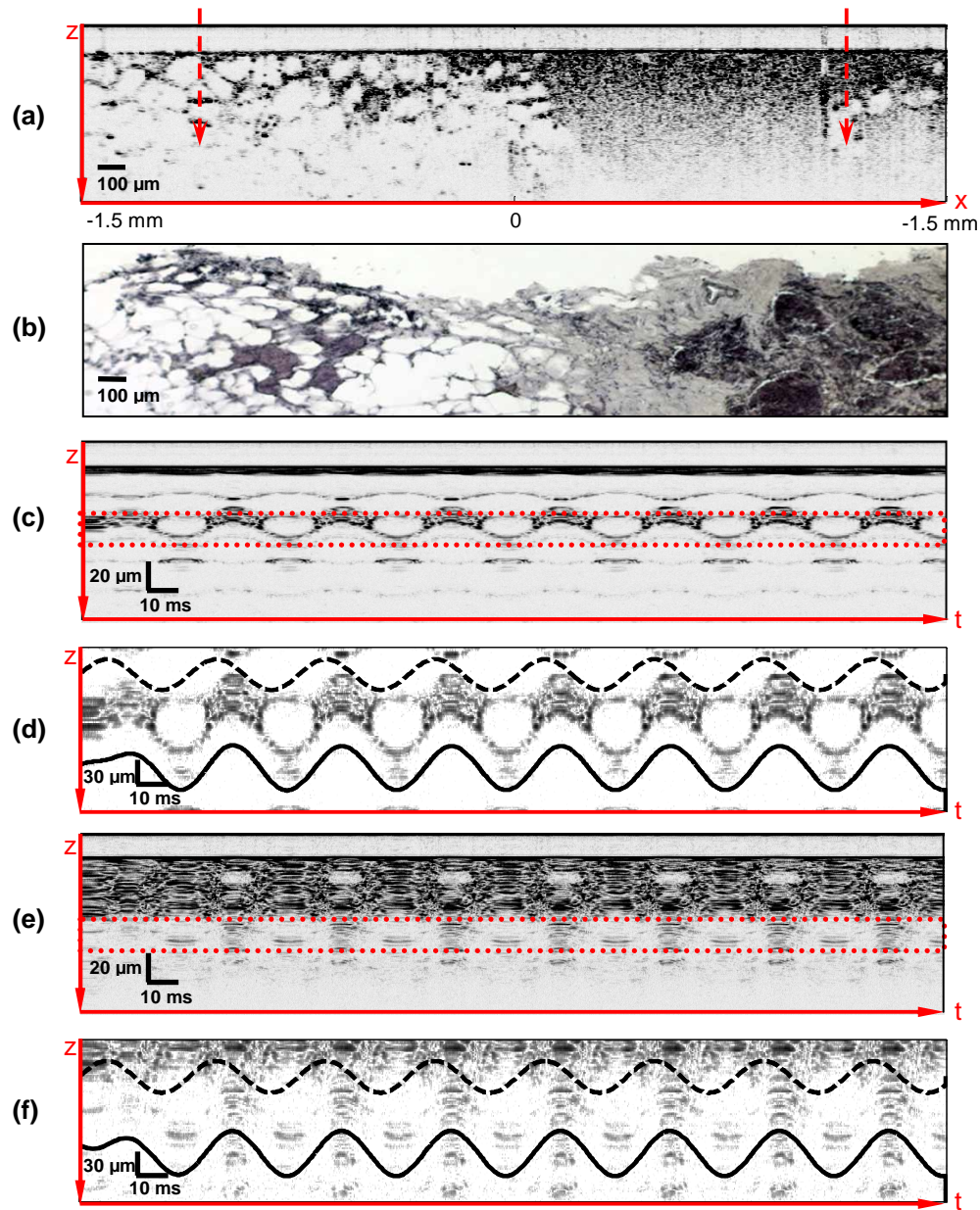
Fig. 5. OCE of human breast tissue. (a) B-mode OCT image of breast tissue. The left side of this image represents the adipose tissue while the right side of the image represents the tumor tissue. Dotted arrows denote the two positions which have corresponding OCE images. (b) Histology image corresponding to (a). (c) M-mode sinusoidally-driven OCE image of the breast tissue at the laser beam position on the left side in (a). (d) Magnified image of the dotted range in (c). The dotted line represents the driving wave form and the solid line represents the fitted curve, while the one between them is the real particle motion track. (e) M-mode sinusoidally-driven OCE image of the breast tissue at the laser beam position on the right side in (a). (f) Magnified image of the dotted range in (e). The dotted line represents the driving wave from and the solid line represents the fitted curve, while the one between them is the real particle motion track.

One can observe in Fig. 6 that the results from the phase-resolved OCE method correspond with the amplitude-based OCE results of Table 2 and the apparent regions of tumor and adipose within the structural OCT image. The elasticity map allows for the differentiation of the tumor from the normal adipose on the micro-scale. Furthermore, elasticity differences on the tumor side of the OCE map (differentiated by yellow and green colors) are observed, which cannot be differentiated on the OCT structural image alone. In comparison with histology, we can see that these elasticity differences are likely due to the presence of fibroblasts and tumor cells comprising the tumor tissue. This ability to differentiate small biomechanical variations on the micro-scale may offer the potential for early-stage tumor detection, where it is often difficult to differentiate tissue types by the optical scattering properties alone, and certainly when these changes are too small to be detected by more traditional ultrasound or MR elastography techniques, or by palpation. Currently, however, our mechanical model does not account for the couplings between tissue regions with different elastic moduli, and thus, the values on the elasticity map represent relative values of the elastic moduli of the tissue. Further refinement of these models could account for these couplings and improve the quantification of these measurements.
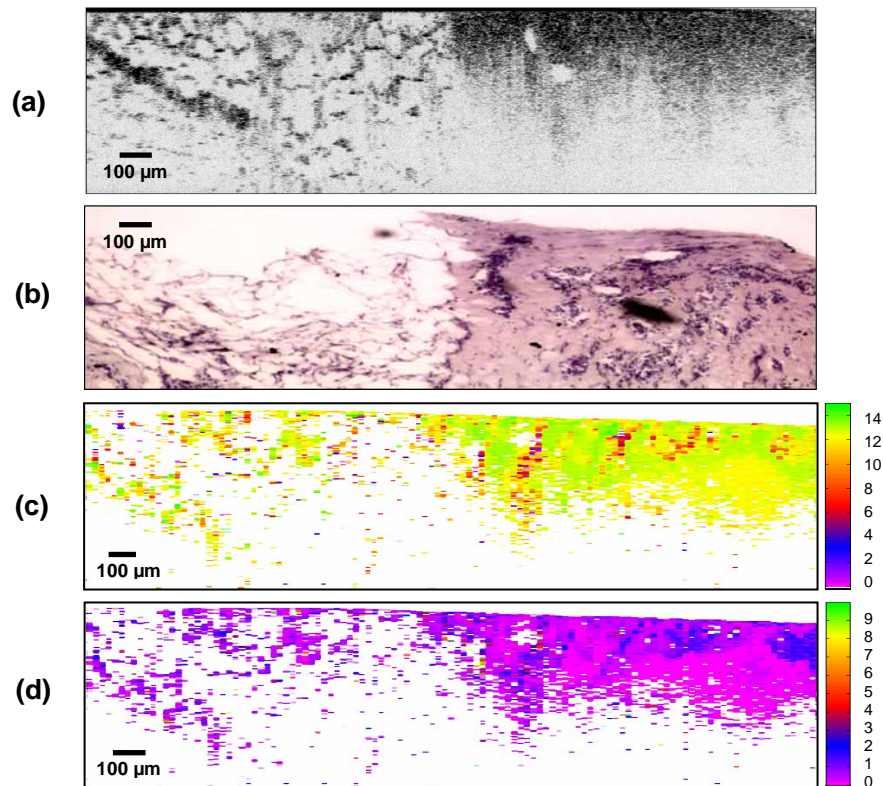

Fig. 6. Phase-resolved OCE map of human breast tissue elasticity. **a,** B-mode OCT image of breast tissue. The left side of this image represents the adipose tissue while the right side of the image represents the tumor tissue. **b,** Histology image corresponding to **a**. **c,** Map of elasticity by sinusoidally-driven phase-resolved OCE. **d,** Error map of elasticity by sinusoidally-driven phase-resolved OCE. Unit for color bar is kPa.

3.3 System sensitivity

From our results on silicone tissue phantoms, we note that the measurements from the step-driven OCE, sinusoidally-driven OCE, and standard indentation method are slightly different, likely due to differences in the applied strain rate in these methods. It has been previously shown that the elastic modulus of a biological sample is dependent on the strain rate of its deformation, due to resistance originating from organic matrices in the sample [33]. Thus, for the tissue phantoms and the human tissues, the larger the strain rate, the larger the measured elastic modulus. With strain rates much larger than those used in the indentation method, the elastic moduli measured by OCE can be treated as dynamic elastic moduli. These can then be associated with the static elastic moduli according to the linear relationship shown in Fig. 4. In the range of 15 to 250 kPa, we find the relationship of $E_s > E_m > E_i$ (where E_i represents the elastic modulus measured by indentation method). In our research, the indentation method strain rate is fixed at 10 μm/s while the OCE strain rate is varying for different samples. For sinusoidally-driven OCE, the strain rates range approximately from 3 mm/s to 17 mm/s for different samples. For step-driven OCE, the strain rate is as high as approximately 30 mm/s, but decreasing over the time of the measurement due to the exponential decay. This explains why the sinusoidally-driven OCE is more closely matched with the indentation method. Due to the relatively large strain rate and its rapidly changing nature in step-driven OCE, compared to the indentation method used to validate OCE, this method is not recommended and was not used for the subsequent tissue measurements.

   System sensitivity is a critically important parameter to characterize the potential of the OCE system measurement. In our dynamic system, the sensitivity can be described by the output error, which is the product of the output sensitivity function and parameter error [34]. We estimated the error from fitting boundaries for the measured parameters, and then calculated the output error for the elastic moduli. According to equations for E_s and E_m, the absolute elastic modulus output error in step-driven OCE is given by

$$\sigma_{Es} = \sqrt{\left(\frac{\partial E}{\partial \lambda}\right)^2 \sigma_\lambda^2 + \left(\frac{\partial E}{\partial \mu}\right)^2 \sigma_\mu^2} = (2\frac{L_0}{S}m')\sqrt{\lambda^2\sigma_\lambda^2 + \mu^2\sigma_\mu^2} \ , \qquad (7)$$

while in sinusoidally-driven OCE, the expression is

$$\sigma_{Em} = \sqrt{\left(\frac{\partial E}{\partial \lambda}\right)^2 \sigma_\lambda^2 + \left(\frac{\partial E}{\partial \alpha}\right)^2 \sigma_\alpha^2}$$

$$= (2m'\omega\frac{L_0}{S})\sqrt{\left(\frac{1}{\tan\alpha}\right)^2 \sigma_\lambda^2 + \left(\lambda\frac{\sin^2\alpha}{\cos^4\alpha}\right)^2 \sigma_\alpha^2} \ , \qquad (8)$$

assuming that the measurement errors of m, S, L_0, and ω are negligible. The estimates of the absolute elastic moduli output error were shown in Table 1. It can be seen that the relative output error can be as small as 0.08% for the step-driven method. However, the output error for sinusoidally-driven OCE is larger than for the step-driven method and the error from the human tissue is worse than from the tissue phantoms. This is because in sinusoidally-driven OCE, the coefficient of viscosity is relatively too small to be accurately fitted, compared with dominant driving waves. Thus, fitting of the step-driven OCE data usually had a higher R-squared value than for the sinusoidally-driven OCE data, and the sensitivity was subsequently better in the former method. The silicone tissue phantoms used in these studies have TiO_2 microparticles in them as optical scatterers, so extracting particle tracking data by the spline algorithm is more straightforward than in human tissue, in which a single scatterer motion track can sometimes be difficult to extract, such as in the example shown for the neoplastic human breast tissue. The majority of tissues probed by optical imaging modalities such as

OCT are optically heterogeneous, thereby facilitating our ability to locate and track single scatterers for this method.

4. Conclusion

Micro-scale mapping and quantitative measurements of biomechanical properties have been obtained from tissue phantoms and biological tissues (normal and neoplastic human breast tissue) using a novel dynamic OCE system and methodology. This system utilizes low-frequency dynamic mechanical waves to drive tissue and measures elastic moduli based on solutions to wave equations. Speckle tracking methods, which are used widely in conventional elastography studies, are not needed in this system, avoiding the deficiencies associated with speckle tracking. Results from this OCE system have been calibrated with biomechanical tissue models, and validated against a standard indentation method for determining elastic modulus. Furthermore, by using phase-resolved displacement measurements, we computed a biomechanical property distribution map and showed the ability to differentiate tumor and normal regions of *ex vivo* human breast.

This novel OCE system exhibited high resolution in both axial and transverse directions in accordance with OCT technology, and sensitivity in the elastic modulus as high as 0.08%. Thus, quantitative measurement, micro-scale resolution, high sensitivity, and dynamic wave excitation (without speckle tracking) are the main features for this novel optical technique that enables spatial determination and mapping of biomechanical properties. With these features and associated *in vivo* OCT imaging, our novel OCE technology has potential to perform more accurately and with higher resolution in various biomedical imaging applications that are optically accessible. This OCE technology may also contribute to understanding the micro-scale biomechanical tissue properties during the growth and development of engineered and natural biological tissues, and the biomechanical responses of these tissues following the application of mechanical or pharmacological stimuli.

Additional studies are needed to further improve this system. More accurate tissue models such as finite element models can be developed, instead of the mass-weighted Voigt model, for different tissue imaging applications. Using this current methodology, every pixel in the OCE image or biomechanical map requires wave equation fitting and as a result, the processing time is currently too long for real-time applications. Fortunately, these current computational limitations will be overcome as computing power continues to improve. Current efforts are investigating more efficient computational algorithms to increase the image processing speed and filter out normal biological tissue motion that will be expected in *in vivo* studies.